



Input of IBA for the study of plasmonic properties of doped ZnO nanocrystals

B. Canut, B. Masenelli, Y. Zhang, A. Apostoluk, C. Bernard, S. Daniele, D. Müller

► To cite this version:

B. Canut, B. Masenelli, Y. Zhang, A. Apostoluk, C. Bernard, et al.. Input of IBA for the study of plasmonic properties of doped ZnO nanocrystals. Nuclear Instruments and Methods in Physics Research Section B: Beam Interactions with Materials and Atoms, 2020, 479, pp.74-79. 10.1016/j.nimb.2020.06.021 . hal-02881433

HAL Id: hal-02881433

<https://hal.science/hal-02881433>

Submitted on 21 Jun 2022

HAL is a multi-disciplinary open access archive for the deposit and dissemination of scientific research documents, whether they are published or not. The documents may come from teaching and research institutions in France or abroad, or from public or private research centers.

L'archive ouverte pluridisciplinaire **HAL**, est destinée au dépôt et à la diffusion de documents scientifiques de niveau recherche, publiés ou non, émanant des établissements d'enseignement et de recherche français ou étrangers, des laboratoires publics ou privés.



Distributed under a Creative Commons Attribution - NonCommercial 4.0 International License

Input of IBA for the study of plasmonic properties of doped ZnO nanocrystals

B. Canut^{1*}, B. Masenelli¹, Y. Zhang¹, A. Apostoluk¹, C. Bernard², S. Daniele³,
D. Müller⁴

¹Université de Lyon, F-69000 Lyon, France and INL, CNRS, UMR 5270, INSA Lyon F-69621 Villeurbanne, France.

²Université de Lyon, F-69000 Lyon, France and I2I, CNRS IN2P3, UMR 5822 F-69621 Villeurbanne, France.

³Université de Lyon, C2P2-CPE Lyon, UMR CNRS 5265, F-69616 Villeurbanne, France.

⁴Université de Strasbourg, F-67000 Strasbourg, France and ICUBE, CNRS, UMR 7357 F-67037 Strasbourg, France.

Abstract

In this work, we used ion beam analyses (IBA) to characterize doped ZnO crystalline nanoparticles elaborated by different methods: (i) low energy cluster beam deposition (LECBD) for ZnO:Ga, (ii) metal organic framework (MOF) for ZnO:Li and (iii) sol-gel for ZnO/SiO_x core-shell system.

The analyses were performed either in RBS mode using ⁴He⁺⁺ ions of 6 MeV energy (characterization of Ga and Si) or in NRA mode using ¹H⁺ ions of 2.5 MeV energy (characterization of Li). The experimental data allowed determining the mean concentration of dopants (Ga, Li) or shell atoms (Si) and their areal masses. These elemental information, coupled with structural (TEM, X-ray) and optical (IR spectroscopy, photoluminescence) ones, were of prime importance permitting to better understand the optical properties of doped ZnO nanocrystals.

*Corresponding author:

E-mail : bruno.canut@insa-lyon.fr

Phone : +33 472 438 734

Fax : +33 472 438 531

1. Introduction

A recent and emerging research field aims to extend the plasmonic properties of nano-objects to the mid infrared (MIR) range [1-3]. This would allow the design of chemical sensors of high sensitivity since most of the chemical molecules exhibit vibrational modes in that spectral range. In addition, wavelengths around 1.5 μm correspond to the telecommunication range.

Up to now, the main studied plasmonic systems were based on noble metal nanoparticles (Ag, Au) and have given rise to promising applications in many fields like biological labels and surface-enhanced spectroscopies [4-6]. However, metal particles have plasma frequencies limited to visible range, suffer high losses and are hardly compatible with the conventional technologies of the Si industry [7]. In order to overcome these drawbacks, a promising route consists in processing nanostructures based on degenerated semiconducting oxides like ZnO. This material presents favourable properties for the expected applications (a wide and direct bandgap, large exciton binding energy of 60 meV, biocompatibility) and its plasma resonance could be tuned from the visible to the MIR range by the electron gas concentration and thus by the dopant activation [8-10]. In the referred works the n-doping of ZnO was achieved using Al, Ga or Sn species. Besides, the p-doping of ZnO (for instance with Li) remains a challenge because of self-compensation caused by native defects which behave as donors [11].

Another system taking benefit of the optical properties of ZnO for designing light emitting devices is the nanocomposite ZnO/SiO_x structure. It is well known that pure ZnO nanoparticles can aggregate and that their luminescence suffers from aging effects [12, 13]. Embedding ZnO nanoparticles into SiO_x should stabilize and permit to maintain high emission yield up to an enlarged temperature range and to tune its wavelength (from blue to green) by controlling the density of ZnO/SiO_x interfaces [14].

In this work, we used ion beam analyses (IBA) to characterize doped ZnO nanoparticles elaborated by different methods: (i) low energy cluster beam deposition (LECBD) for ZnO:Ga, (ii) metal organic framework (MOF) for ZnO:Li and (iii) sol-gel for ZnO-PAA/SiO_x core-shell system (PAA = polyacrylic acid).

In these three cases, our objective was to measure the mean concentration of dopants actually present in the samples and possibly to depict the existence of other unwanted species over an extended thickness ($\approx 1 \mu\text{m}$) within a sample. The elemental measurements provided by IBA should allow a better understanding of the optical properties of ZnO-based nanostructures studied in this work.

2. Experimental procedure

2.1 Sample elaboration

The ZnO:Ga nanoparticles have been synthesized by the low energy cluster beam deposition technique (LECBD) detailed elsewhere [15]. A pellet made of a mixture of ZnO and Ga₂O₃ powders annealed at 800°C for 10h was ablated with a high power pulsed (10 Hz repetition rate) YAG:Nd laser. The resulting plasma was quenched in a buffer gas (mixture of 75 % He and 25 % O₂ at 20 mbar) and underwent a supersonic adiabatic expansion while moving to the deposition chamber working at 10⁻⁷ mbar. The obtained nanoparticles (mean size of 5 nm) were deposited on a silicon substrate at a typical rate of 1nm.min⁻¹, leading to a film thickness of several hundred of nm. The nominal values of the Ga content were adjusted between 3 and 9 % by varying the composition of the two initial powders.

The ZnO:Li nanoparticles were prepared using a metal-organic framework (MOF) procedure derived from that proposed by T.G. Glover et al. [16] for the synthesis of Zn-CPO-27 MOF. The zinc precursor Zn(NO₃)₂ · 4H₂O and dihydroxyterephthalic acid (DHTA) were dissolved in dimethylformamide (DMF) using sonication. The insertion of lithium was performed by adding LiNO₃ dissolved in dehydrated ethanol. Three nominal relative concentrations of Li were used : 0.1, 1 and 2.7%. At the end of the chemical processes, the solvents were evacuated, which resulted in obtaining of a Zn/Li-CPO-27 powder. The preparation of ZnO:Li was then performed by annealing this powder at 800°C under air flow using a heating ramp of 5°C.min⁻¹. From SEM observations, the mean size of ZnO:Li crystallites was about 70 nm. For the purposes of ion beam analysis the sample, in powder form, was pressed on a carbon adhesive tape.

The ZnO-PAA/SiO_x core-shell nanoparticle system was elaborated by the sol-gel hydrolysis method. Among the many chemical routes allowing the synthesis of ZnO by this technique [17] the one used to synthesize ZnO-PAA/SiO_x core-shell nanoparticle system used in this study is as follows: ZnO nanoparticles functionalized with the polyacrylic acid (PAA) whose synthesis is described elsewhere [18] were dispersed in ethanol to which an appropriate amount of tetraethoxysilane (TEOS) was added then transferred into the flask and stirred for at 700 rpm at room temperature and for 30 minutes. Then ethanol, water and NH₃·H₂O were then added into the reaction milieu with a mass ratio of 1:0.93:0.027. The mixture consisting of ZnO, TEOS, solvent, and NH₃·H₂O was stirred at 700 rpm for 4 hours and subsequently the products were retrieved by centrifugation, washed twice with ethanol and then dried in a vacuum oven for 4 hours at 70°C. The obtained white powder of ZnO-PAA/SiO_x nanoparticles was then pressed onto a carbon adhesive tape and studied.

2.2 Ion beam analysis techniques

In addition to the microstructural and optical characterizations (transmission or scanning electron microscopies, infrared and photoluminescence spectroscopies), we used ion beam analyses to get information about the actual contents of the different dopants (Ga, Li) or foreign species (SiO_x) of the ZnO nanocrystallites. Measuring the Ga concentration in ZnO by RBS is not a trivial task as the atomic mass of Ga is close to that of Zn. In order to improve the selectivity of the analysis we used a high energy (6 MeV) $^4\text{He}^{++}$ beam delivered by the Van de Graaff accelerator of the Nuclear Physics Institute of Lyon (IPNL). The backscattered particles were detected with a 13 keV resolution implanted junction set at an angle of 172° with respect to the beam axis.

The ion beam analysis of lithium contained in ZnO:Li requires a nuclear reaction due to the low atomic mass of Li. Among the numerous nuclear techniques available [19], we have chosen the particle-particle reaction $^7\text{Li}(p, \alpha)^4\text{He}$ using a proton beam of 2.5 MeV initial energy. The detector geometry was identical to that mentioned previously for the RBS analysis of ZnO:Ga and no absorber foil was used.

Finally, the analyses of ZnO-PAA/ SiO_x samples were performed with conventional RBS, using a $^4\text{He}^+$ beam of 2 MeV energy.

3. Results and discussion

3.1 ZnO:Ga

Figure 1(a) displays the whole RBS spectrum recorded on a sample doped with a nominal Ga concentration of 3 %. A strong resonance on the oxygen signal and an oscillating behavior on the silicon signal are evidenced. These features are due to the non-Rutherford scattering cross-sections σ_{O} and σ_{Si} of these two elements at high energies. From one database to another there is a great dispersion on the energy dependence of σ_{O} and σ_{Si} above 3 MeV. In addition the oxygen signal, which covers a backscattering energy range between 1.5 MeV and 2.2 MeV, overlaps with an additional resonance of the silicon signal which occurs at a backscattering energy of about 2 MeV. For these reasons, it was not possible to fit correctly the experimental data below 3 MeV and to measure with acceptable accuracy the proportion of oxygen in the sample. Therefore we assumed a mean composition $\text{Zn}_{(50\%-x)}\text{Ga}_x\text{O}_{50\%}$ and determined the gallium content x and the areal mass of the deposit from the $\{\text{Zn} + \text{Ga}\}$ signal located in the high energy region of figure 1(a). This signal exhibits a tail at its low energy edge. As the depth diffusion of the clusters in the target must be discarded, this effect can be ascribed to the layer roughness [20]. Knowing that Zn and Ga atoms obey conventional Coulombian cross-sections it was possible to reliably fit the experimental data in 3.5 MeV – 5 MeV energy range. This was performed with the help of the SIMNRA simulation code [21], taking into

account of a surface roughness following a Gamma distribution function. The best fit led to an areal mass of the deposit of $340 \mu\text{g.cm}^{-2}$, corresponding to an equivalent thickness of 600 nm of bulk ZnO which is consistent with the deposition rate parameters used in the present LECBD process. On the other hand, the full width at half maximum of the surface roughness distribution was found to be $300 \mu\text{g.cm}^{-2}$, which is a large value comparable with the areal mass of the layer. A detailed view of the RBS spectrum in the high energy range is presented on figure 1(b). As can be seen, the main isotopes of zinc and gallium are resolved. From the simulation code a mean stoichiometry $\text{Zn}_{47\%}\text{Ga}_{3\%}\text{O}_{50\%}$ was extracted, in a good agreement with the nominal composition. It is worthwhile to notice that the fitting was performed assuming the same $[\text{Ga}]/[\text{Zn}]$ ratio over the entire sample thickness. Due to the large surface roughness, the low energy edges of the gallium isotopes are buried in the tail of the RBS signal. It was thus impossible to measure the maximum depth e_{max} at which gallium atoms are present, let alone determine the concentration profile of these atoms. However, in order to estimate a lower limit of e_{max} , we performed further simulations based on a two-layered target. This latter consisted of a surface layer of composition $\text{Zn}_{47\%}\text{Ga}_{3\%}\text{O}_{50\%}$ and equivalent thickness e , followed by a buried layer of composition $\text{Zn}_{50\%}\text{O}_{50\%}$ extending up to the total equivalent thickness of 600 nm. The results evidenced a clear mismatch between the fit and the experimental data when e becomes lower than 100 nm. This allows to conclude that the mean relative concentration of gallium extracted from RBS data is valid from the surface to a maximum depth exceeding 100 nm.

Figure 2(a) compares the gallium concentrations measured by RBS with the results obtained by X-ray photoelectron spectroscopy (XPS) and by energy dispersion spectroscopy (EDS). In the case of porous nanomaterials, such as those studied in the present work, the depth probed by XPS is about 10 nm. For a given probed depth, the area of the peak corresponding to the detected photoelectron spectrum is directly proportional to the number of atoms present in the probed volume. The coefficient of proportionality is the ionization cross section of Scofield which is accurately known for most of the elements. In order to have access to an absolute analysis, the apparatus transfer function (response) must be established using reference samples. In our case, since the apparatus transfer function was not known, we only gave relative quantification (amount of Ga with respect to Zn). EDS analysis was performed in a JEOL 2010F operating at 200 kV, while collecting TEM images. The detection was performed using 80 mm^2 SSD detector from Oxford Instrument and the analysis was performed using the corresponding software (Aztec) provided by Oxford instrument. For the two lowest nominal doping ratios (namely 3 % and 6 %) the concentrations measured by the three techniques are similar, permitting to conclude that the incorporation of gallium is homogeneous at least over the first 100 nm (RBS gives a mean Ga concentration in this thickness range, while XPS probes only the first 10 nm). Besides, one can note a significant disagreement between the RBS and

XPS results related to the highest nominal doping (9 %) and strong variations in the Ga content from one particle to another (EDS results). As mentioned in our previous paper [10], this is probably due to an evolution versus time of the target ablation which induces a depth evolution of the Ga concentration. The plasmonic properties of ZnO:Ga samples were evidenced by Fourier transform infrared reflectivity (FTIR). The obtained spectra exhibited a broad band whose minimum could be tuned from 4 μm (2500 cm^{-1}) to 3 μm (3300 cm^{-1}) by the gallium concentration [10, 22]. Using a procedure based on Drude and Bruggemann models, it was possible to extract from FTIR data the free carrier concentration n_e for the three used doping levels. In order to get quantitative information about the doping efficiency the obtained n_e values were divided by the atomic concentration n_{Ga} of gallium deduced from RBS analyses. As shown in figure 2(b), only 10 % of the incorporated Ga atoms effectively contribute to the free electron gas. Many factors could be responsible for this low activation efficiency: incorporation of gallium on non-substitutional sites or even segregation at the surface of the nanoparticles, the presence of crystalline defects which trap some of free electrons, formation of $\text{Ga}_{\text{Zn}}\text{-V}_{\text{Zn}}$ acceptor complexes which act as compensation centers. It is worth noticing that this last contribution can be significantly reduced by working in a poor O environment during the ablation process [23].

3.2 ZnO:Li

Figure 3 displays the photoluminescence (PL) spectra recorded on undoped and Li-doped ZnO samples elaborated by MOF. The PL spectrum of pure ZnO consists of a broad asymmetrical peak with maximum at about 500 nm and a small ultraviolet emission below 400 nm. Emission contributions due to interstitial zinc I_{Zn} or to interstitial oxygen I_{O} , expected at 427 and 413 nm, respectively [24, 25] are not evidenced. This indicates that the MOF process induces the formation of only vacancies defects in ZnO rather than interstitial defects. The global PL signal can be satisfactorily deconvoluted using different components related to zinc vacancies V_{Zn} emitting at 398 nm [26, 27] and oxygen vacancies V_{O}^+ , V_{O}^{2+} and V_{O} which emission is located at 510, 590 and around 700 nm, respectively [28, 29]. The PL spectra recorded on ZnO:Li do not exhibit any longer the sharp UV emission peak at 400 nm resulting from the exciton recombination. This behavior, already evidenced elsewhere [30], is probably due to a degradation of the crystalline quality of the samples when doped with Li. Another consequence of the presence of lithium, which is only significant at the highest nominal doping level (2.7 %), is a slight increase of the luminescence yield between 550 nm and 700 nm. According to Wang et al. [31], Li cannot cause directly any emission in ZnO, but acts

as a defect mediator by changing the balance between the intrinsic defects O_i and V_O which emit in the above-mentioned wavelength range.

An example of IBA analysis, performed on a sample doped with a nominal concentration of 2.7 % Li, is presented on figure 4. The results obtained on a reference sample (bulk LiNbO_3) probed in the same conditions are also given for comparison. On the same spectrum one can evidence below 2.5 MeV the backscattering events on Zn, Nb, O and Li atoms and below 7.5 MeV the nuclear reaction events related to the $(p \alpha)$ reaction on Li atoms. Note that the RBS signal corresponding to Li is only visible on the LiNbO_3 reference, due to the low concentration of this element in ZnO:Li . The pile-up contribution, extending up to 4.4 MeV, is a well-known artifact resulting from the very high counting rate of backscattered H^+ ions in comparison with the counting rate of the emitted α particles. The lithium content in ZnO:Li was assumed to be constant in depth. It was determined by measuring at maximum energy of the emitted α particles (7.45 MeV) the heights H_{LiNbO_3} and $H_{\text{ZnO:Li}}$ of the spectra recorded on LiNbO_3 and ZnO:Li targets, respectively. These heights are proportional to the relative concentration of lithium (0.2 for LiNbO_3 and x for ZnO:Li) and inversely proportional to the nuclear reaction stopping cross-sections $\epsilon_{\text{LiNbO}_3}$ and $\epsilon_{\text{ZnO:Li}}$ of LiNbO_3 and ZnO:Li targets, respectively. The proportionality factor is the same in both cases, as the two spectra were recorded in identical conditions (the same integrated charge of the incident ions, the same geometry of detection and the same energy per channel). In the present analysis conditions, the reaction factor is close to zero and the stopping cross-section of 2.5 MeV $^1H^+$ ions is much lower than the stopping cross-section of 7.45 MeV $^4He^{++}$ ions in both targets. For these reasons the nuclear reaction stopping cross-sections $\epsilon_{\text{LiNbO}_3}$ and $\epsilon_{\text{ZnO:Li}}$ are practically equal to the stopping cross-section of 7.45 MeV $^4He^{++}$ ions in LiNbO_3 and ZnO:Li , respectively. Using the Bragg rule (the contribution of Li atoms was not taken into account for the slowing-down in ZnO:Li) we obtained $\epsilon_{\text{LiNbO}_3} = 42 \times 10^{-15} \text{ eV.cm}^2$ and $\epsilon_{\text{ZnO:Li}} = 25 \times 10^{-15} \text{ eV.cm}^2$. Using these values and by measuring the ratio between H_{LiNbO_3} and $H_{\text{ZnO:Li}}$ an average composition $[\text{Li}]/[\text{Zn}] = 0.3 \%$ was found. This relative concentration of lithium is by one order of magnitude lower than the expected one. Similar discrepancies were found for the two other nominal doping levels of 1 % and 0.1 %. In these two other cases the compositions measured by IBA were found to be 0.05 % and 0.03 %, respectively. This would explain why the PL spectra for ZnO:Li described above show so few changes compared to the spectrum related to pure ZnO .

3.3 ZnO-PAA/SiO_x

Figure 5 shows a TEM image of a nanocomposite ZnO-PAA/SiO_x. The dark contrast indicates the presence of ZnO clusters having an average size of ≈ 4 nm. These clusters are very well separated from each other. This can be attributed to the presence of SiO_x which is known to prevent any aggregation process [32, 33]. The mean composition of the nanocomposite was measured by RBS analysis. For this purpose the sample, initially in powder form, was deposited on a carbon adhesive tape. A typical result is presented on Figure 6. Within the RBS accuracy, no elements other than Zn, Si and O could be detected in the thickness probed by the analysis (≈ 1 μ m). The signal related to the presence of carbon in the PAA is not clearly resolved due to the low scattering cross-section of this element in the present analysis conditions and to a probable desorption process which occurs in polymers when analyzed with ion beams in the MeV range [34]. One can note in addition the poor energy resolution (35 keV) which can be due to charging effect of the target and to ionoluminescence. Despite these pitfalls it was possible, with the help of SIMNRA simulation code (see the fitting drawn in figure 6), to extract from the RBS spectrum a mean atomic composition Zn_{25%}O_{67%}Si_{8%}. A more accurate comparison between the experimental and simulated data shows a slight zinc depletion (- 2 %) and a concomitant excess of silicon (+ 2 %) near the surface. This composition gradient occurs up to a maximum areal mass of about 40 μ g.cm⁻², corresponding to an equivalent thickness of 70 nm for bulk ZnO. The mean atomic composition mentioned above could correspond to a mixing of (ZnO)_y and (SiO₂)_{1-y} species with $y = 76$ %. This y value, chosen to match the ratio $[\text{Zn}]/[\text{Si}] = 25/8 = 3.1$ measured from RBS data, agrees reasonably with the nominal composition of the two oxides which is controlled during the elaboration process. However, y underestimates the ratios $[\text{O}]/[\text{Si}] = 67/8 = 8.4$ and $[\text{O}]/[\text{Zn}] = 67/25 = 2.7$, measured also from RBS data. One possible explanation is that excess oxygen atoms evidenced by RBS are present in the chemical bonds of the non-desorbed polymer.

Figure 7 displays the PL spectra recorded at different temperatures on a ZnO-PAA/SiO_x sample with a nominal relative concentration of 20 % of SiO_x. According to A. Mikrajuddin et al. [35], in the probed wavelength range the contribution of SiO₂ to the PL yield is negligible. The broad feature extending in the visible range with a maximum located around 550 nm can be ascribed to the different intrinsic defects in ZnO (see § 3.2). In addition the surface passivation with PAA should enhance the formation of non-polar facets of ZnO which are beneficial to the visible emission [18]. At increasing temperatures up to 140°C, the intensity of the emission band decreases, without any significant shift of its components. This result can be explained by higher rates of non-radiative recombinations at elevated temperatures. With a view to achieving a light emitting diode built from ZnO-PAA/SiO_x it is of the first importance to control its behavior in the long term. Many works showed that the green emission of ZnO materials, especially when synthesized using sol-gel, decreases due to aging or to

thermal stress [36]. In order to address this question, following PL spectroscopy performed at 140°C, new spectra were recorded after returning to room temperature. As shown in figure 8(a), the recovery of initial luminescence at 24°C is not complete. The maximum of the emitted intensity (at $\lambda = 550$ nm) is about 76 % of its original value. As shown in figure 8(b), a higher degradation of the PL intensity with temperature and a recovery percentage of only 65 % are evidenced when the same experimental procedure is performed on ZnO-PAA sample without SiO_x. This promising result, although preliminary, highlights the beneficial effect of SiO_x coating to improve the stability of an optical device based on ZnO nanoparticles.

4. Conclusion

In this work we showed that ion beam analyses have led to a deeper understanding of the optical properties of ZnO-based nanostructures. The coupling of RBS and FTIR results obtained on ZnO:Ga samples allowed to determine the percentage of gallium (here 10 %) responsible for the plasmonic properties. In the case of ZnO:Li, nuclear reaction analysis was found to be sensitive enough to detect very low lithium concentrations (below 0.5 %). The values obtained, ten times lower than the nominal ones, could explain why only a very slight increase in the emission yield could be detected in the doped sample between 550 and 700 nm. Finally, RBS analysis allowed measuring the mean ratio y between ZnO and SiO_x in ZnO-PAA/SiO_x targets. In a future systematical work this capability would allow to depict an optimal y value conciliating good emissive properties in the visible range and low aging effects in these samples elaborated by the sol-gel method.

References

- [1] X. Liu, M.T. Swihart, Chem. Soc. Rev. **43** (2014) 3908-3920.
- [2] A. Comin, L. Manna, Chem. Soc. Rev. **43** (2014) 3957-3975.
- [3] R. Stanley, Nature Photonics **6**(7) (2012) 409-411.
- [4] E. Ozbay, Science **311**(5758) (2006) 189-193.
- [5] S.A. Maier, M.L. Brongersma, P.G. Kik, S. Meltzer, A.A. Requicha, H.A. Atwater, Advanced Materials **13**(19) (2001) 1501-1505.
- [6] A.R. Halpern, R.M. Corn, ACS Nano **7**(2) (2013) 1755-1762.
- [7] G.V. Naik, V.M. Shalaev, A. Boltasseva, Advanced Materials **25**(24) (2013) 3264-3294.
- [8] R. Buonsanti, A. Llordes, S. Aloni, B.A. Helms, D.J. Milliron, Nano letters **11**(11) (2011) 4706-4710.
- [9] G.V. Naik, J. Liu, A.V. Kildishev, V.M. Shalaev, A. Boltasseva, Proceedings of the National Academy of Sciences **109**(23) (2012) 8834-8838.
- [10] M.K. Hamza, J.-M. Bluet, K. Masenelli-Varlot, B. Canut, O. Boisron, P. Melinon, B. Masenelli, Nanoscale **7** (2015) 12030-12037.
- [11] J.C. Fan, K.M. Sreekanth, Z. Xie, S.L. Chang, K.V. Rao, Progress in Materials Science **58** (2013) 874-985.
- [12] F.K. Shan, B.I. Kim, G.X. Liu, J.Y. Sohn, W.J. Lee, B.C. Shin, Y.S. Yu, J. Appl. Phys. **95**(9) (2004) 4772-4776.
- [13] J. Bang, H. Yang, P.H. Holloway, Nanotechnology **17**(4) (2006) 973-978.
- [14] Y.Y. Peng, T.E. Hsieh, C.H. Hsu, Nanotechnology **17**(1) (2006) 174-190.
- [15] D. Tainoff, B. Masenelli, O. Boisron, G. Guiraud, P. Melinon, J. Phys. Chem. C **112** (2008) 12623-12627.
- [16] T.G. Glover, G.W. Peterson, B.J. Schindler, D. Britt, O. Yaghi, Chemical Engineering Science **66** (2011) 163-170.
- [17] L. Znaidi, Materials Science and Engineering B **174** (2010) 18-30.
- [18] Y. Zhu, A. Apostoluk, P. Gautier, A. Valette, L. Omar, J.M. Bluet, K. Masenelli-Varlot, S. Daniele, B. Masenelli, Scientific Reports **6** (2016) 23557.
- [19] J. Räisänen, Nucl. Instr. and Meth. B **66** (1992) 107-117.
- [20] S.U. Campisano, G. Ciavola, E. Costanzo, G. Foti, E. Rimini, Nucl. Instr. and Meth. **149**(1-3) (1978) 229-233.

- [21] M. Mayer, SIMNRA Users Guide, Report IPP 9/113, Max-Planck- Institut für Plasmaphysik, Garching, Germany (1997).
- [22] M.K. Hamza, PhD thesis Lyon (2017).
- [23] M.K. Hamza, O. Boisson, B. Canut, P. Melinon, J. Penuelas, M. Gendry, B. Masenelli, RSC Adv. **7** (2017) 28677-28683.
- [24] K. Bandopadhyay, J. Mitra, RSC Adv. **5** (2015) 23540-23547.
- [25] A. Zubiaga, J.A. Garcia, F. Plazaola, F. Tuomisto, K. Saarinen, J. Zuniga Pérez, V. Munoz-Sanjose, J. Appl. Phys. **99** (2006) 053516.
- [26] F. Tian, X. Zhang, Y. Chen, Chem. Lett. **45** (2016) 388-390.
- [27] K.T. Roro, J.K. Dangbegnon, S. Sivaraya, A.W.R. Leitch, J.R. Botha, J. Appl. Phys. **103** (2008) 053516.
- [28] K.C. Barick, D. Bahadur, J. Nanosci. Nanotechnol. **7** (2007) 1935-1940.
- [29] K.H. Tam, C.K. Cheung, Y.H. Leung, A.B. Djuricic, C.C. Ling, C.D. Beling, S. Fung, W.M. Kwok, W.K. Chan, D.L. Phillips, L. Ding, W.K. Ge, J. Phys. Chem. B **110** (2006) 20865-20871.
- [30] H.P. Hsu, D.Y. Lin, C.Y. Lu, T.S. Ko, H.Z. Chen, Crystals **8** (2018) 228-235.
- [31] M. Wang, F.J. Kim, S.H. Hahan, J. Lumin. **131** (2011) 1428-1433.
- [32] A.E. Raevskaya, A.G. Milekhin, D.R.T. Zahn, Ya V. Panasiuk, N.A. Yeryukov, O.L. Stroyuk, L.A. Sveshnikova, S. Ya Kuchmiy, E.E. Rodyakina, V.M. Dzhagan, V.F. Plyusnin, RSC Adv. **4** (2014) 63393-63401.
- [33] H. Chamroukhi, Z. Ben Hamed, A. Telfah, M. Bassou, A. Zeinert, R. Hergenroder, H. Bouchriha, Optical Materials **84** (2018) 703-713.
- [34] F. Nayamar, J.I. Budnick, Nucl. Instr. and Meth. in Phys. Res. **B15** (1986) 285-287.
- [35] A. Mikrajuddin, F. Iskandar, K. Okuyama, F.G. Shi, J. Appl. Phys. **89** (2001) 6431-6434.
- [36] Y. Li, L. Xu, X. Li, X. Shen, A. Wang, Appl. Surf. Sci. **256** (2010) 4543-4547.

Figure captions

Figure 1: (a) RBS analysis of a ZnO:Ga sample with a nominal concentration of 3 % of Ga. A zoom of the high energy edge of the spectrum is presented in (b). Analysis conditions: $^4\text{He}^{++}$ ions of 6 MeV energy; detection angle: 172° . The solid curves are fittings of the {Zn + Ga} signal using SIMRA simulation code.

Figure 2: (a) Comparison between the Ga doping percentages measured by different techniques and (b) doping efficiency n_e/n_{Ga} versus the Ga doping measured by RBS. The solid curves are drawn to guide the eye.

Figure 3: Photoluminescence spectra recorded at 300K on undoped (a) and Li-doped (b) ZnO samples elaborated by MOF. Doping level: 2.7 % (nominal value). Excitation wavelength: $\lambda = 266$ nm.

Figure 4: IBA analysis spectrum of a ZnO:Li sample doped with a nominal concentration of 2.7 % of Li (a). The results obtained on bulk LiNbO_3 probed in the same conditions are also given for comparison (b). Analysis conditions: $^1\text{H}^+$ ions of 2.5 MeV energy; detection angle: 172° .

Figure 5: TEM micrograph of ZnO nanocrystals (red circles) in a matrix of PAA and SiO_x .

Figure 6: RBS analysis of a ZnO-PAA/ SiO_x sample. Nominal ratio of the two oxides: $[\text{SiO}_x]/[\text{ZnO}] = 20$ %. Analysis conditions: $^4\text{He}^+$ ions of 2 MeV energy; detection angle: 172° . The solid curve is a fit of the spectrum using SIMRA simulation code.

Figure 7: Photoluminescence spectra recorded at different temperatures on a ZnO-PAA/ SiO_x sample. The dotted curve corresponds to the PL spectrum recorded after returning to room temperature. Excitation wavelength: $\lambda = 266$ nm.

Figure 8: Temperature evolution of the relative intensity at maximum with (a) and without (b) SiO_x coating. The solid curves are drawn to guide the eye. The two horizontals indicate the recovery values at room temperature (see text).

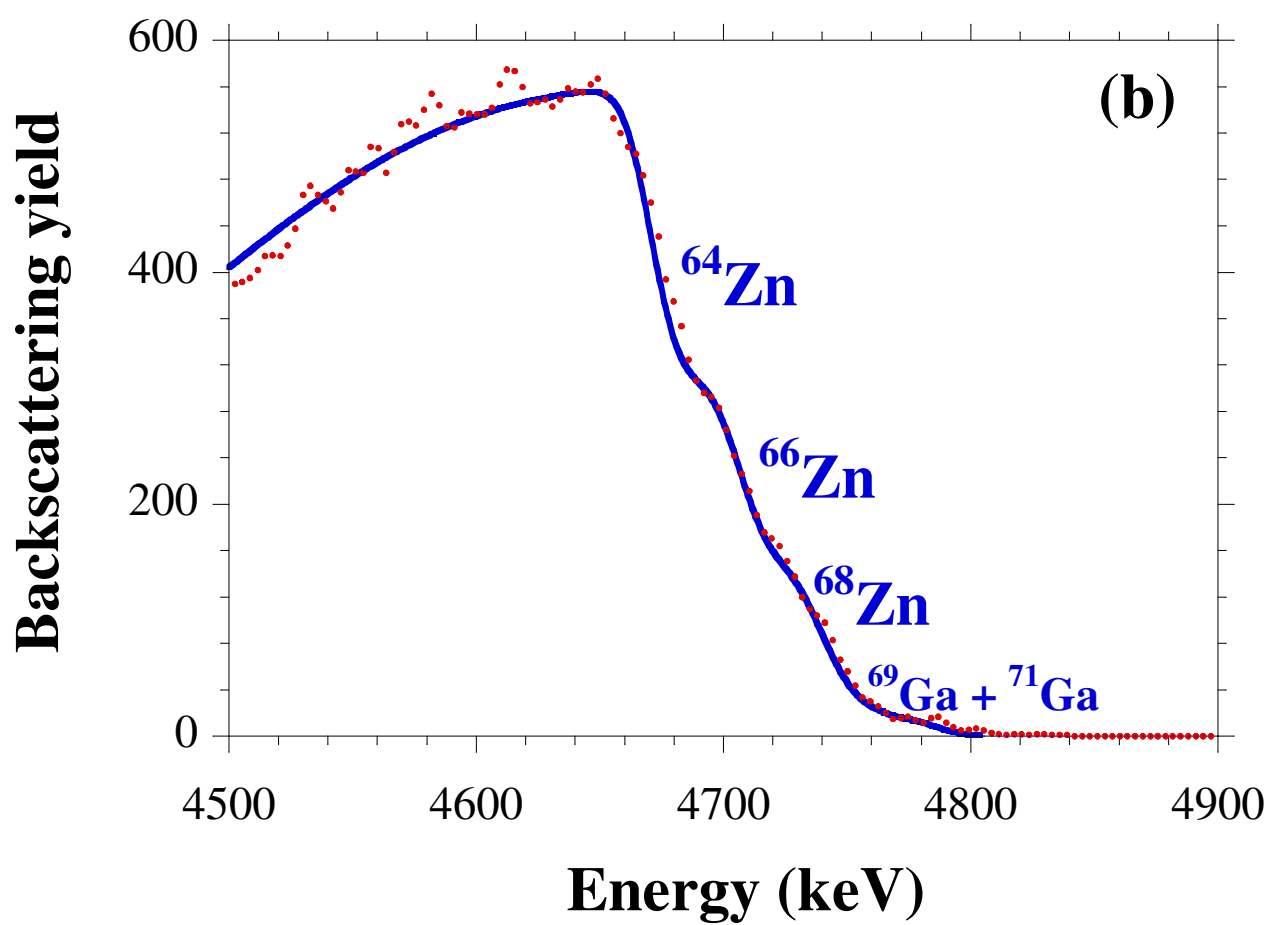
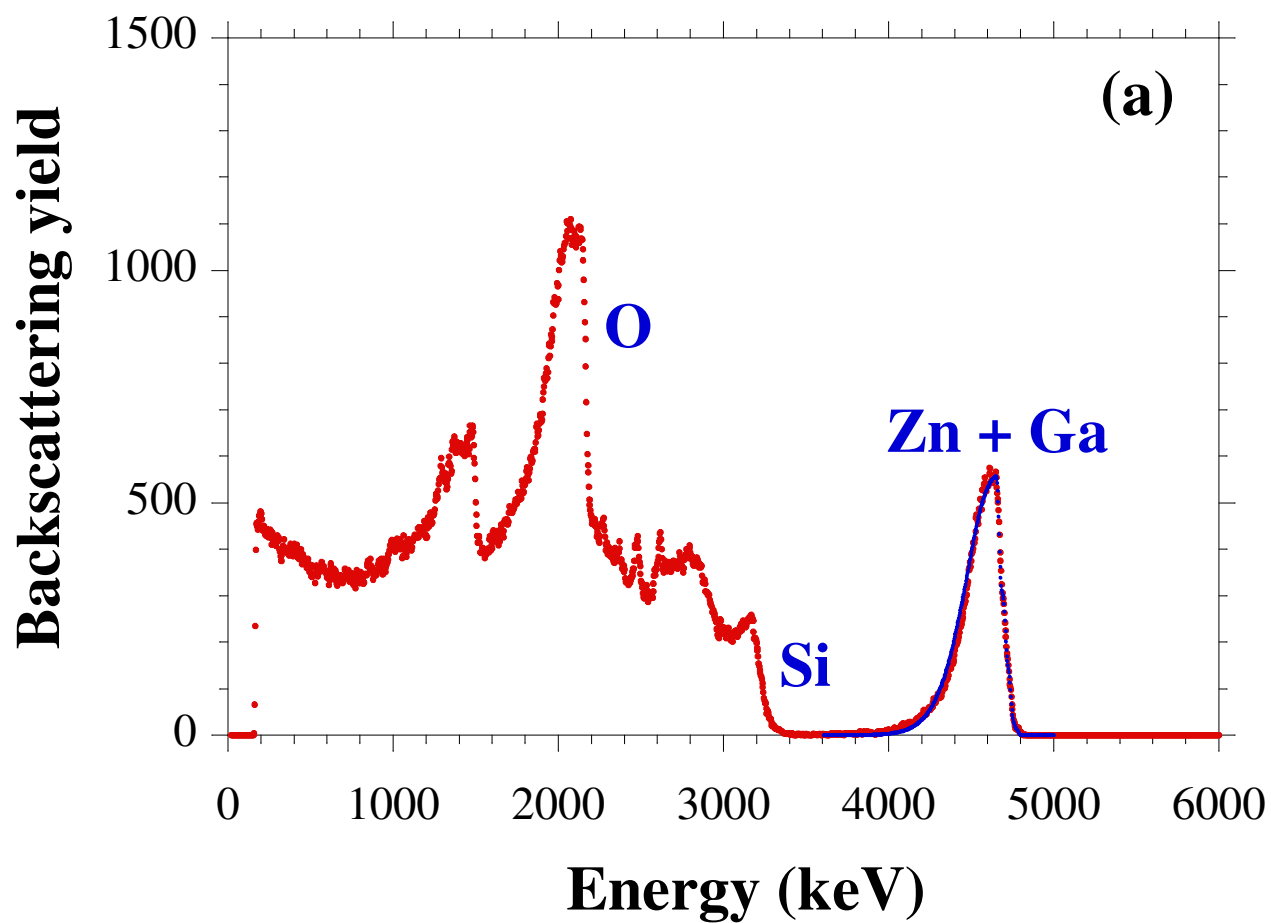


Figure 1

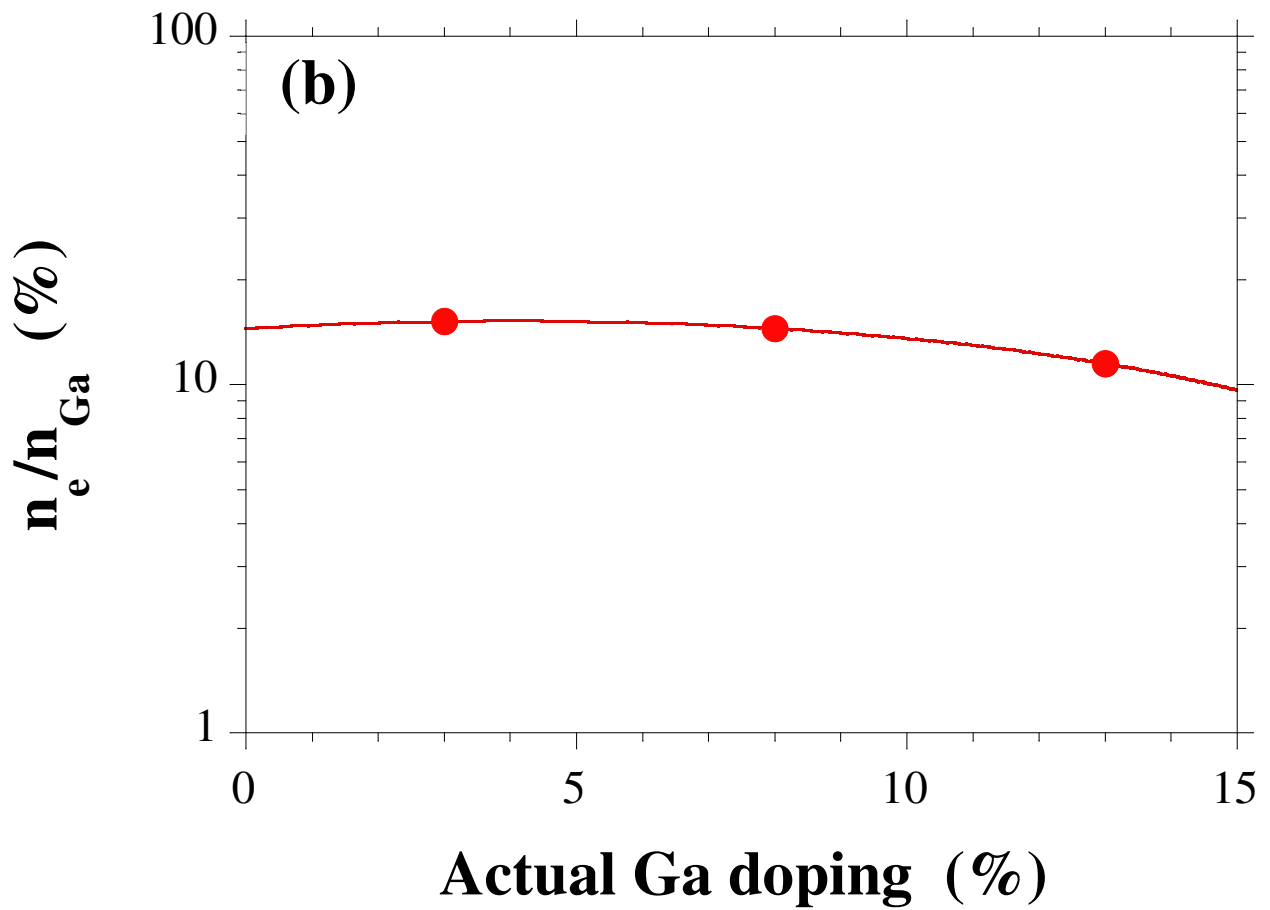
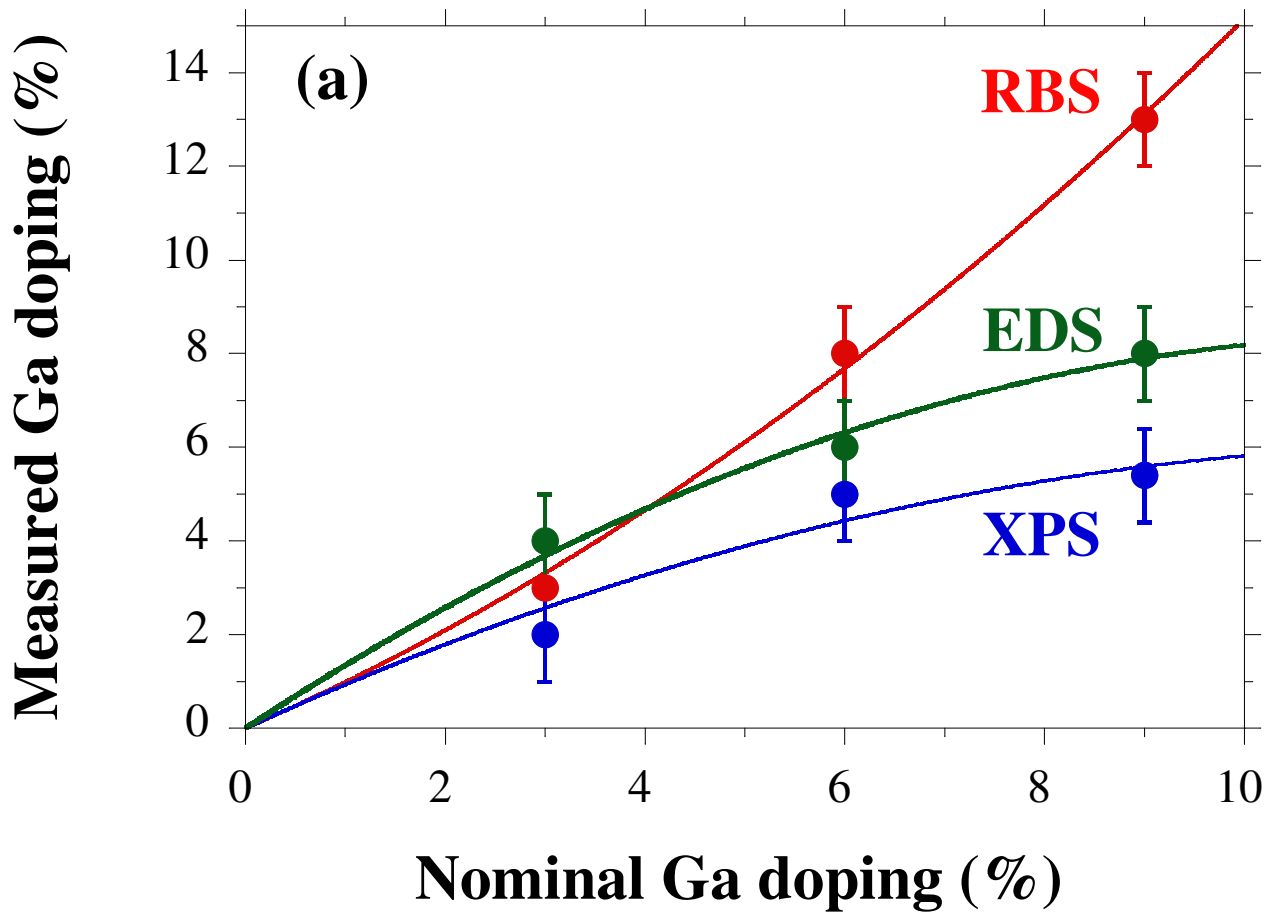


Figure 2

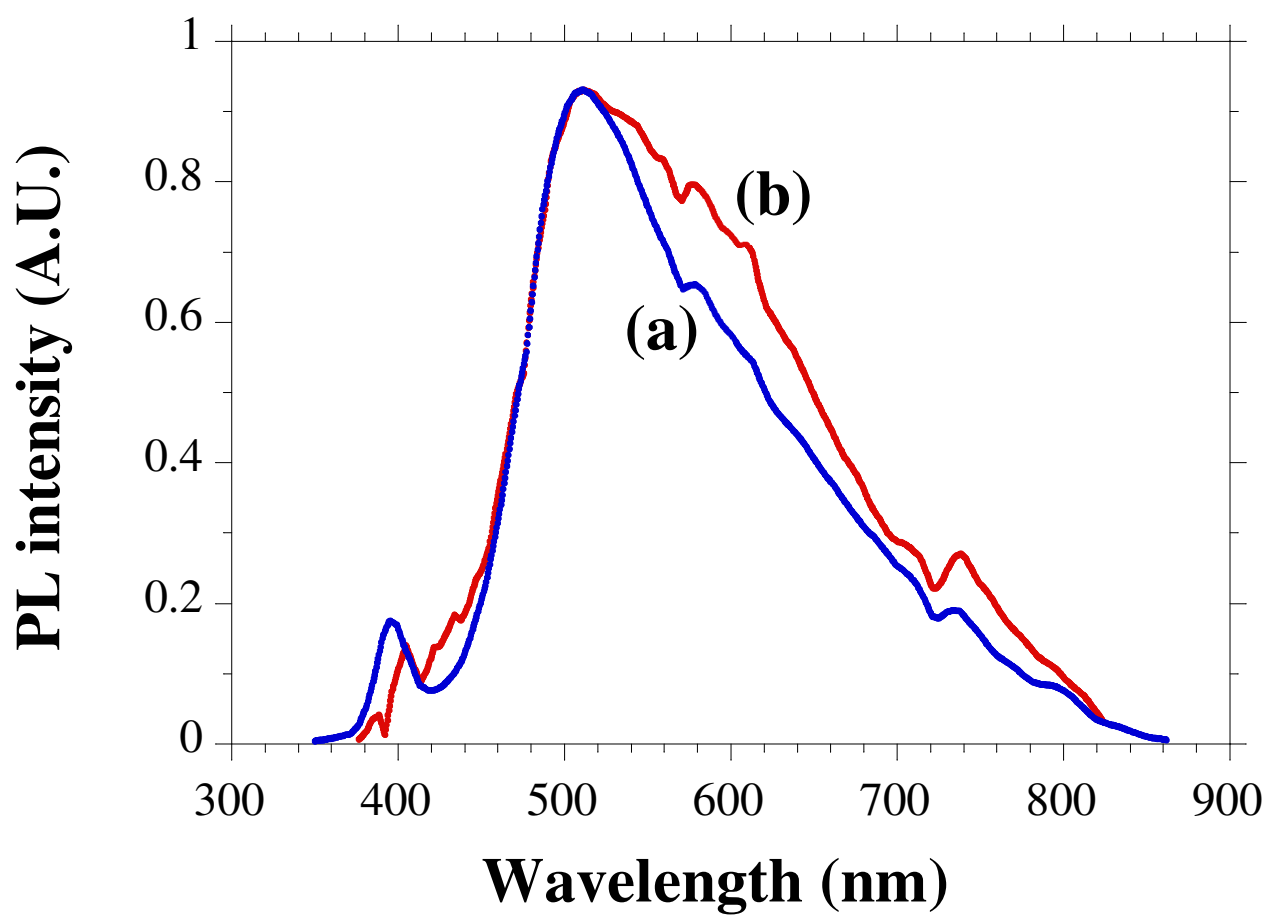


Figure 3

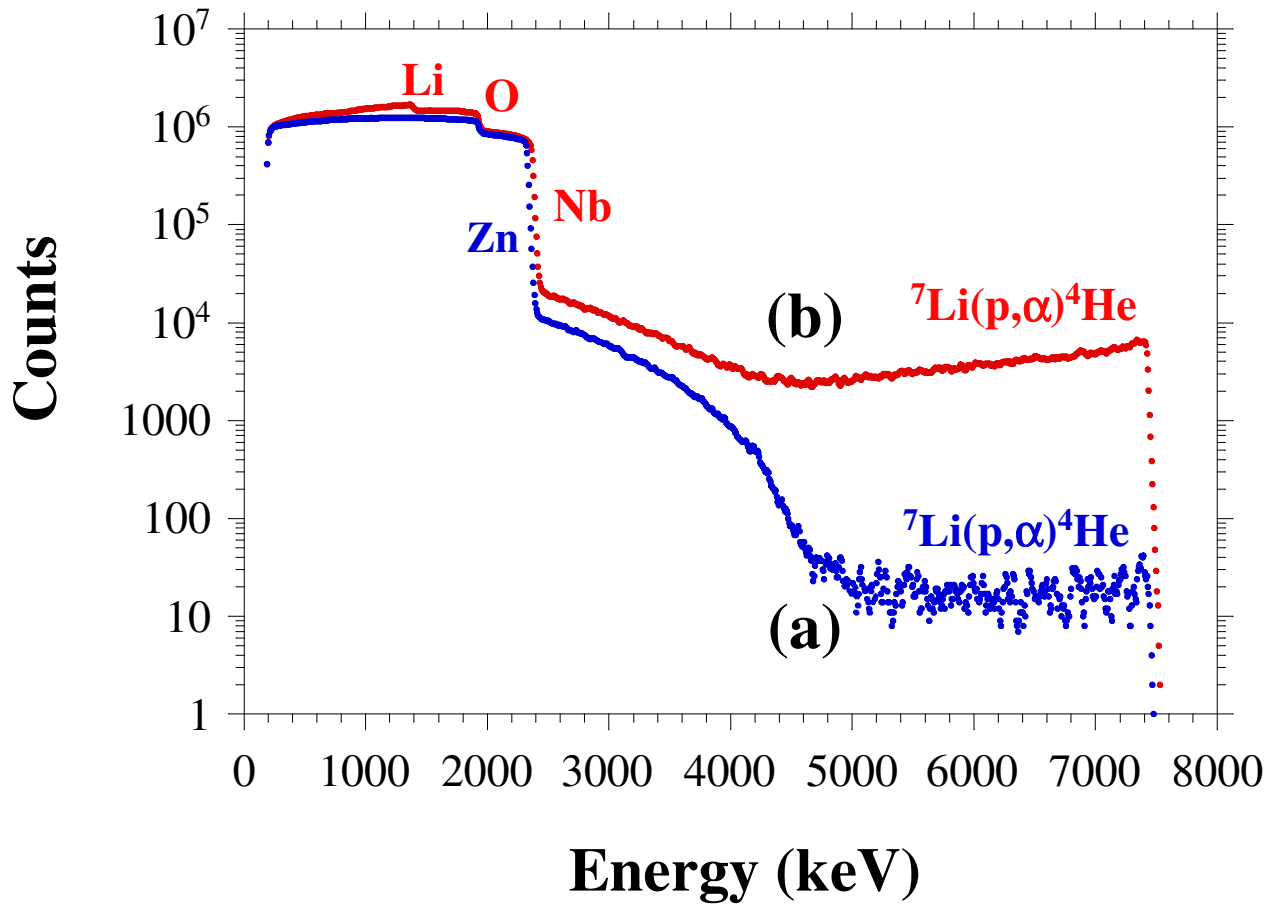
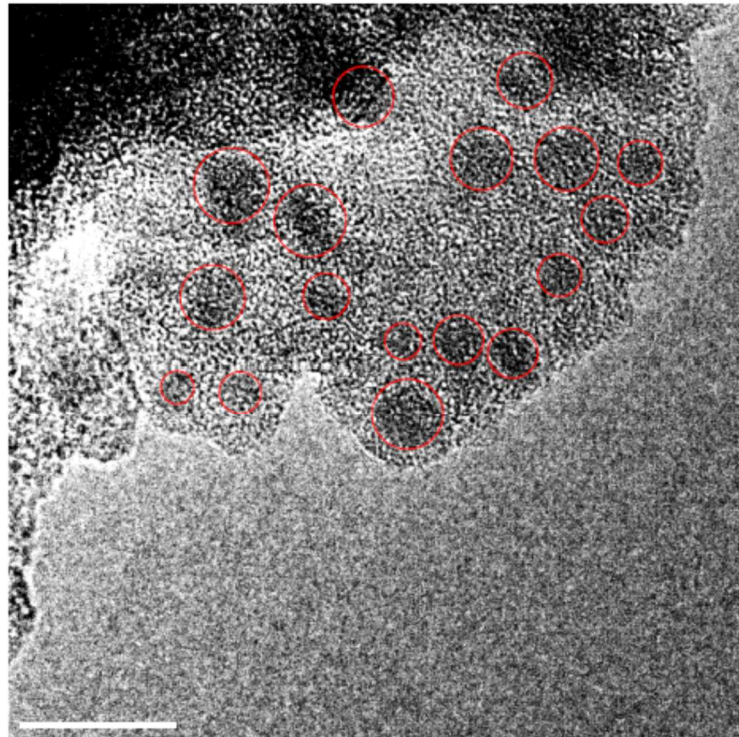


Figure 4



scale bar: 10 nm

Figure 5

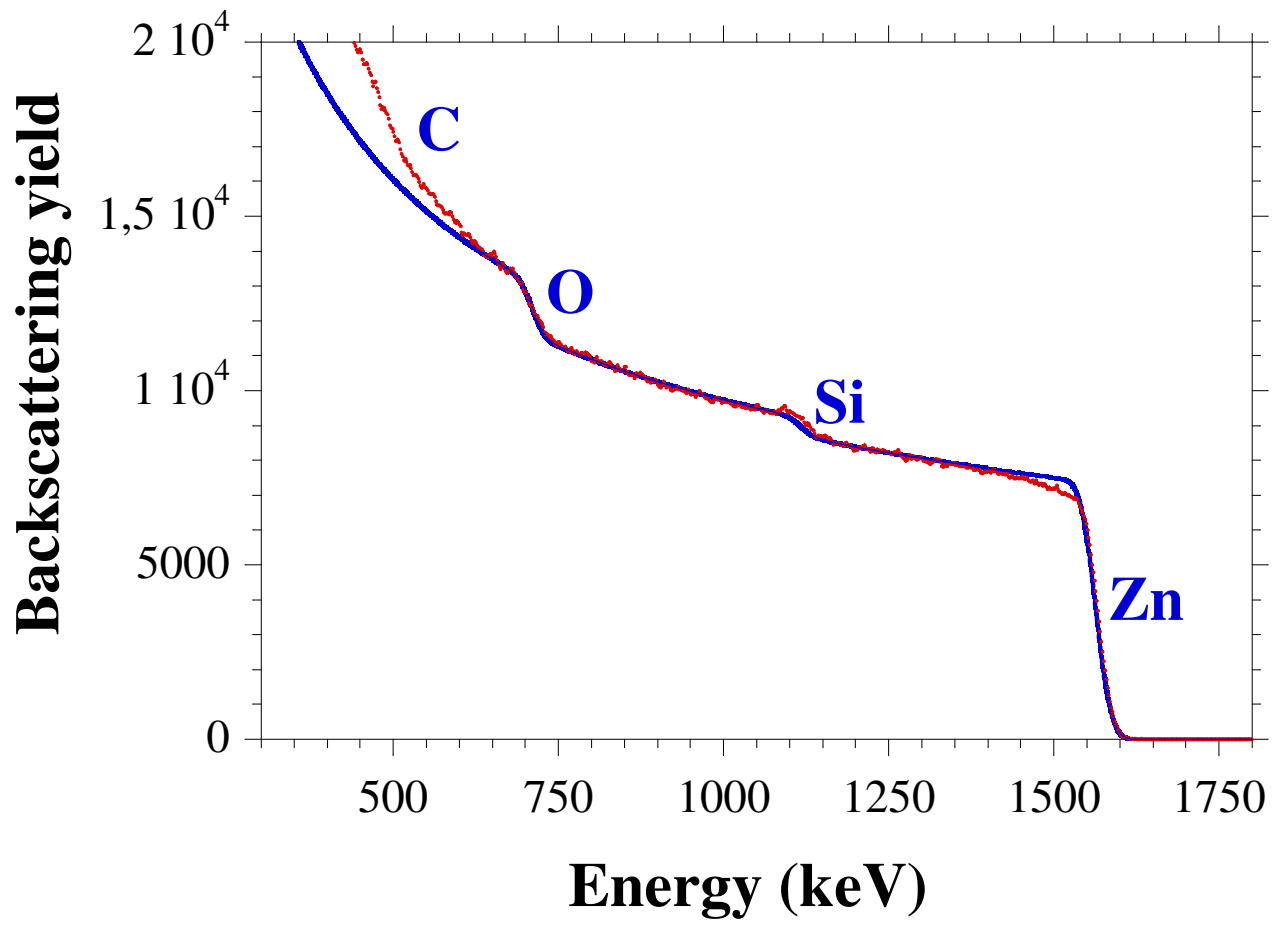


Figure 6

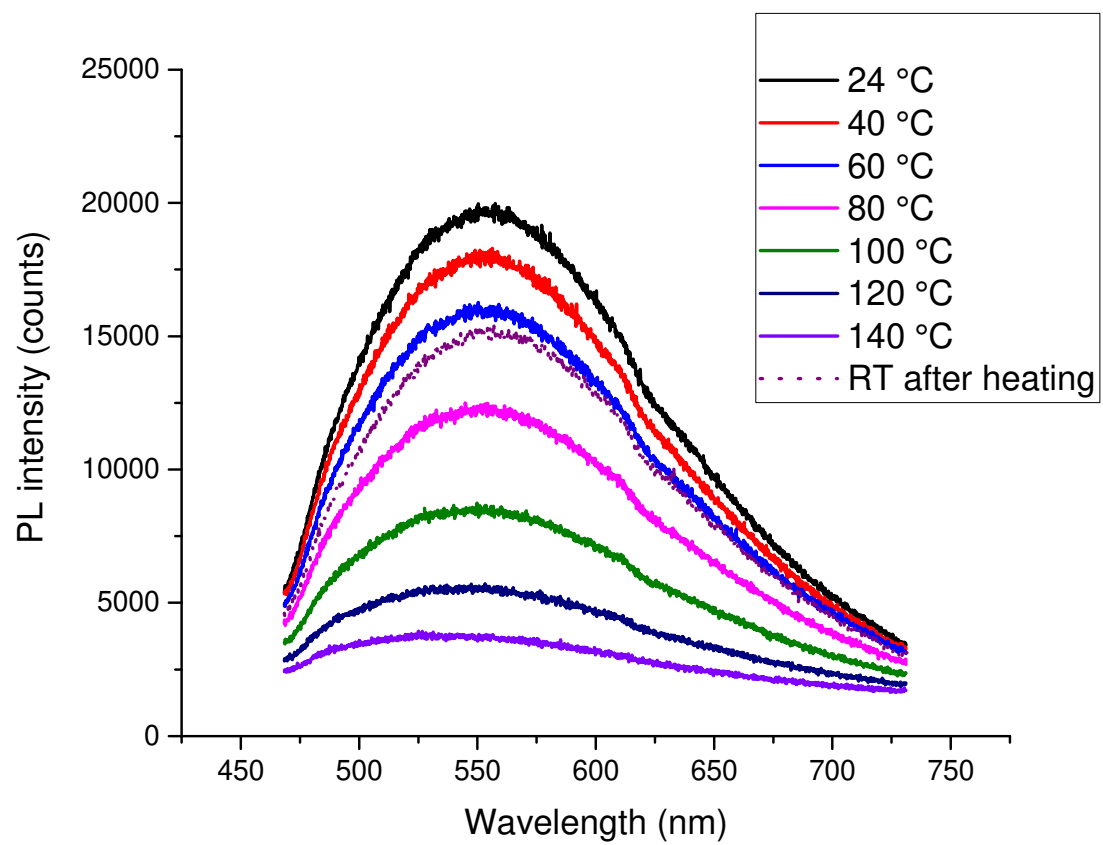


Figure 7

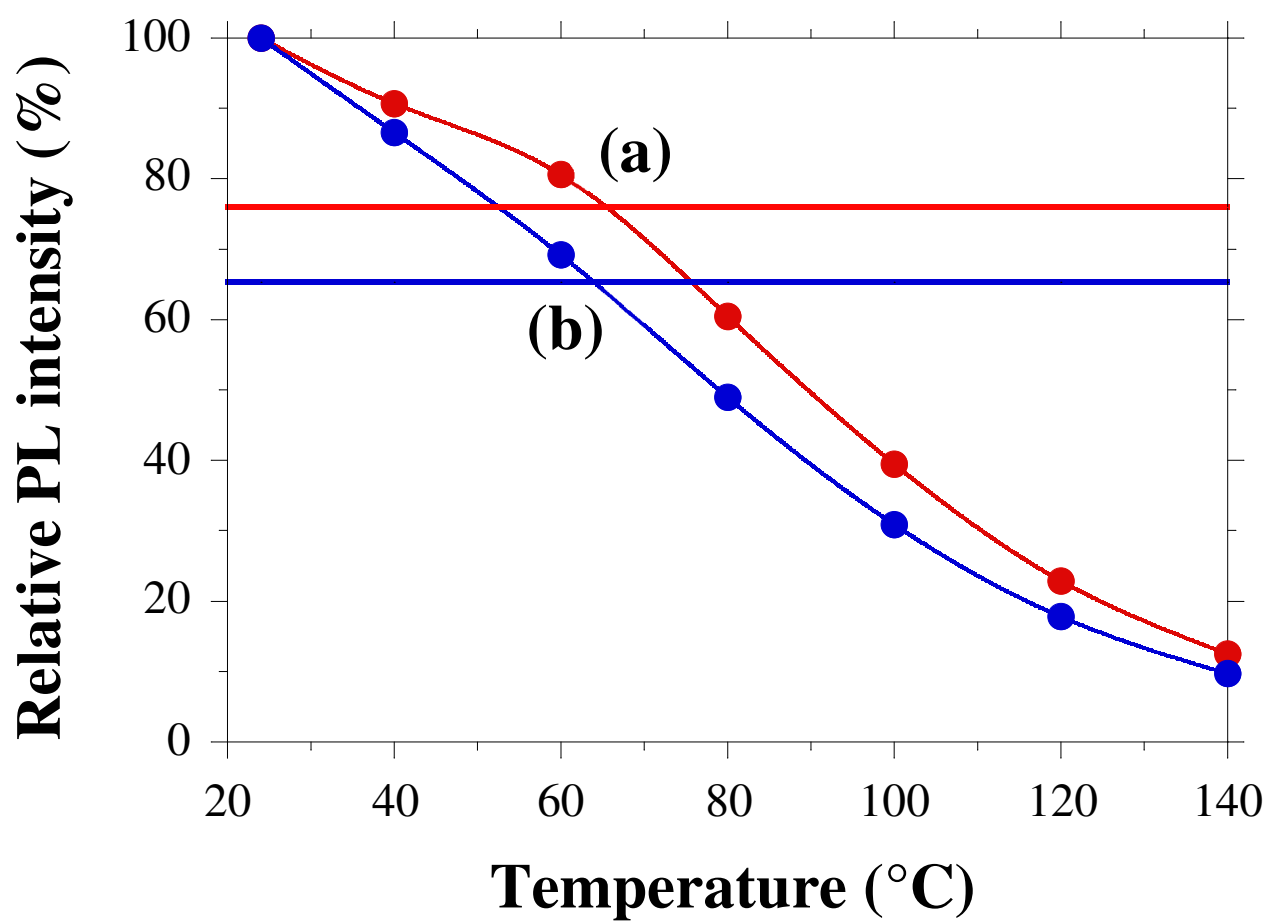


Figure 8